Prod. Eng. Res. Devel. (2014) 8:51–61
DOI 10.1007/s11740-013-0509-8

PRODUCTION PROCESS

Energy dissipation in laser-based free form heading: a numerical approach

Mischa Jahn · Heiko Brüning · Alfred Schmidt · Frank Vollertsen

Received: 20 August 2013 / Accepted: 29 October 2013 / Published online: 14 November 2013

Abstract Cold forming generally allows the fast generation of parts with very low tolerances. In addition, mechanical properties are improved, if work hardening materials are used. Transferring the cold forming process to micro range leads to a decrease in the maximum achievable upset ratio so that the forming process becomes inefficient. Therefore, a laser-based free form heading process has been developed to generate preforms which can be calibrated in a secondary cold forming step. The achievable upset ratios reach values of several hundreds instead of 2.1 which is common for single step mechanical upsetting. In this article, heat losses arising in the material accumulation process using laser-based free form heading are analyzed and discussed. For this purpose, the process is modeled within the framework of continuum mechanics and simulated by a finite element method. By using a numerical approach, a systematic study on heat losses is performed in order to identify the influence of radiation, heat transfer due to convection and thermal conduction during laser irradiation time. The simulation results, which are validated with experimental data, show that the radiation is the most important mechanism reducing the efficiency of the accumulation process.

Keywords Laser micro machining · Micro forming · Miniaturization · Finite element simulation

M. Jahn (✉) · A. Schmidt
Zentrum für Technomathematik (ZeTeM), Universität Bremen, 28359 Bremen, Germany
e-mail: mischa@math.uni-bremen.de

H. Brüning · F. Vollertsen
Bremer Institut für angewandte Strahltechnik (BIAS), 28359 Bremen, Germany
e-mail: bruening@bias.de

1 Introduction

In modern production engineering, miniaturization is of growing interest. Unfortunately, with increasing miniaturization, methods and processes used in macro-scale are sometimes no longer applicable to very small work-pieces, making the production of micro-components a challenging task [9]. Different examples for cold forming processes generating micro-components are existing such as micro backwards extrusion [6] or open die upsetting of cylindrical specimens with diameters <1 mm [13].

Conventionally, a multi-stage cold forming approach is applied to the work-piece in macro-scale, in order to upset a certain length l_0 of a sample with diameter d_0 and forming it simultaneously. Unfortunately, the upset ratio $s := \frac{l_0}{d_0}$ achievable by these methods is very limited and decreases, if d_0 does [13].

Therefore, a two-stage cold forming process with an initial material accumulation step for metallic components in micro-range has been developed within the Collaborative Research Center (CRC) 747 "Micro Cold Forming".

The efficiency of the material accumulation process is highly dependent on the energy available for the melting of material. Therefore, an overview of heat losses arising in laser-based free form heading during irradiation time is given in this paper. This allows for a better understanding of the stability of the process and for finding possible areas of improvement in efficiency. After a description of the laser-based free form heading material accumulation process in Sect. 2, the process is modeled in Sect. 3. A simplified analytical model is used for a rough approximation of the process [20]. For a precise simulation of the process and an analysis of the heat losses arising during the melting

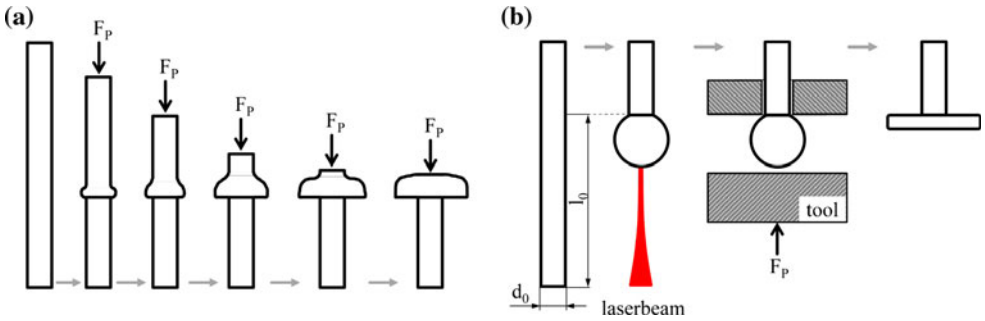

Fig. 1 Conventional multi-stage cold forming process (**a**) and two-stage cold forming process using laser-based free form heading (**b**)

process, the material accumulation process is modeled within the framework of continuum mechanics [4]. Numerical aspects of the finite element method [11] are briefly presented in Sect. 4 and the experimental setup is described in Sect. 5. In Sect. 6, numerical results are compared to experimental data and a parameter variation is performed to analyze energy dissipation effects.

2 Process

Laser beam energy is used to heat up the tip of a metallic rod until it exceeds its melting temperature so that the end of the rod melts. Due to the fact that the diameter of the rod is in the magnitude of one millimeter or smaller, forces related to the surface tension dominate over gravitational forces. The surface tension causes the molten part of the rod to attain a nearly spherical shape which sticks to the rod. This molten part is called preform. After solidification, the preform can be formed by an upsetting process. The maximum achievable upset ratio is reached, as soon as the gravitational force acting on the melt exceeds the surface tension so the preform drips off the rod. Using laser-based free form heading, upset ratios of several hundreds can be reached [17].

The metallic rod and the laser beam are oriented parallel to gravitational force. The laser beam is placed perpendicular to the face surface of the rod. Rod and focus plane are both kept fixed during the accumulation process. When the laser beam heats the rod, a certain part of the rod melts, changing its geometry from cylindrical to nearly spherical. When heating continues, the sphere expands also orthogonal to the laser beam direction and thus its surface moves out of the focus layer causing a so-called defocussing effect [15]. This can be diminished by appropriately feeding of the rod [16] or shifting the laser beam corresponding to the movement of the sphere. For the energy pulses, respectively the upset ratios, considered in this paper, the influence of laser beam defocussing can be neglected according to the results presented in [18].

The experimental investigations shown in this paper are carried out with rods of chromium nickel steel 1.4301 (X5CrNi18-10) with diameters of 0.5 mm as wrought material. The diameters of the preforms are measured with a micrometer caliper with an uncertainty of 1 µm. The volume is calculated by assuming that the preforms are spherical. Figure 1 shows both, the conventional multi-stage upsetting process and the two-stage cold forming process using laser-based free form heading.

3 Mathematical models

3.1 Analytical model

A simplified analytical model describing the laser melting is presented in [19]. This model gives the basis for an understanding of the process and is set up to estimate the energy needed to generate a preform of a certain volume by assuming adiabatic conditions. Therefore, it is assumed that neither heat dissipation from the spherical part of the rod to the ambiance nor within the rest of the rod takes place. This means that any incoupled laser beam energy is used to heat up the part of the rod that forms the preform after the accumulation. Furthermore it is assumed that the material which is heated up reaches but does not exceed melting temperature. All material characteristics are thought to be temperature-independent. According to [5], the absorption coefficient α_L is 0.38. The analytical model relates molten volume V_S of the preform and absorbed energy E_L by

$$E_L = \alpha_L V_S \rho \left(c_{p_s} (T_M - T_0) + H_M \right). \quad (1)$$

The descriptions of the material properties and their values are given in Table 1 (see table footer). For a more feasible approximation of the process, the parameter α_L can be adjusted to consider heat losses empirically, cf. Sect. 6.

3.2 Continuum mechanical model

For a more precise simulation of the material accumulation process, a continuum mechanical model is needed. This model includes laser heating, thermal conduction in the melt and the bulk, radiation described by the Stefan-

Table 1 Material properties of steel 1.4301 (X5CrNi18-10) [14]

T_0	293 K	Initial temperature
T_a	293 K	Ambiance temperature
T_m	1673 K	Melting temperature
ρ	7,900 kg/m^3	Density
c_{p_s}	500 J/kg K	Specific heat capacity in solid
c_{p_l}	830 J/kg K	Specific heat capacity in melt
λ_s	15 J/mK	Thermal conductivity in solid
λ_l	35 J/mK	Thermal conductivity in melt
H_M	276,000 J/kg	Latent heat
μ[1]	5.5×10^{-3} Ns/m^2	Dynamic viscosity
γ[1]	1.872 N/m	Surface tension
β[1]	10^{-4} 1/K	Coefficient of thermal expansion
α_L	0.38	Absorption coefficient

[1] For unknown material properties, the corresponding values of iron [8] are used instead

Boltzmann law, forced convection caused by shielding gas which cools the materials surface and solid-liquid-solid phase transitions. Furthermore, the dynamics in the melt and its free capillary surface evolution have to be considered. Therefore, the Stefan problem is coupled with the Navier–Stokes equations including a free capillary surface. Both, the Stefan problem, cf. for example [1] and [7], and the Navier–Stokes equations with a capillary surface, see e.g. [3], have a long history in material science as well as in pure and applied mathematics, and have been discussed in many publications. However, coupling both problems has been discussed much less, e.g. [4], and is still challenging due to the interdependence of geometry and the solid-liquid-interface.

In the continuum mechanical model [4] some assumptions are made in order to simplify matters: Firstly, material parameters are assumed to be constant for each subdomain that are indicated by the index l for liquid and s for solid. Secondly, vaporization effects are neglected and the melt is assumed to be incompressible so the fluid dynamics can be described by using the incompressible Navier–Stokes equations. The buoyancy effects are modeled by the Boussinesq approximation.

Let $\Omega(t) = \Omega_s(t) \cup \Omega_l(t) \cup \Gamma_S(t) \subset \mathbb{R}^3$ be the time dependent domain for $t \in [t_0, t_f]$, consisting of a solid subdomain $\Omega_s(t)$ which is the rod, a liquid subdomain $\Omega_l(t)$ which is the melt, and a solid-liquid interface $\Gamma_S(t)$. The outer domain boundary $\partial\Omega(t) = \Gamma_C(t) \cup \Gamma_R(t) \cup \Gamma_N(t)$ is distinguished in disjoint sets $\Gamma_C(t), \Gamma_R(t)$ and $\Gamma_N(t)$, with different boundary conditions. Thereby, $\Gamma_C(t)$ denotes the free capillary surface of the melt. Initially, the rod is completely solid, thus $\Omega_l(0) = \emptyset, \Gamma_S(0) = \emptyset$ and $\partial\Omega(0) = \Gamma_R(t) \cup \Gamma_N(t)$. A sketch of the different domains and their boundaries is given in Fig. 2.

The process is modeled by coupling the Stefan problem in the whole domain for the temperature $T: \Omega(t) \to \mathbb{R}$ with the incompressible Navier–Stokes equations in the melt $\Omega_l(t)$ with a capillary surface for the velocity field of the fluid $u: \Omega_l(t) \to \mathbb{R}^3$ and its pressure $p: \Omega_l(t) \to \mathbb{R}$. Using material parameters given in Table 1 and the characteristic numbers given in Table 2, the model is given in non-dimensional units by the PDE-system

$$\begin{aligned} &\partial_t u + u \cdot \nabla u - \nabla \cdot \left(\frac{1}{\mathrm{Re}} \mathrm{D}(u) - p \mathrm{I_d} \right) \\ &\quad = -\frac{\mathrm{Bo}}{\mathrm{We}} e_2 + \frac{\mathrm{Gr}}{\mathrm{Re}^2} T e_2 \qquad \text{in } \Omega_l(t), \end{aligned} \tag{2}$$

$$\nabla \cdot u = 0 \qquad \text{in } \Omega_l(t), \tag{3}$$

$$\partial_t T + u \cdot \nabla T - \frac{1}{\mathrm{RePr}} \Delta T = 0 \qquad \text{in } \Omega_l(t), \tag{4}$$

$$\partial_t T - \frac{1}{\mathrm{RePr}} \frac{\lambda_s \rho_l c_{p_l}}{\lambda_l \rho_s c_{p_s}} \Delta T = 0 \qquad \text{in } \Omega_s(t), \tag{5}$$

with $\mathrm{D}(u) := \nabla u + (\nabla u)^T$. For numerical convenience, the temperature is scaled so that melting temperature corresponds to $T = 0$. The boundary conditions on the free capillary surface are given by

$$u \cdot v = V_{\Gamma_C} \cdot v \quad \text{on } \Gamma_C(t), \tag{6}$$

$$\sigma v = \frac{1}{\mathrm{We}} K v \quad \text{on } \Gamma_C(t), \tag{7}$$

with V_{Γ_C} denoting the velocity of the free boundary, K is the sum of the principle curvatures and $\sigma := \frac{1}{\mathrm{Re}} \mathrm{D}(u) - p \mathrm{I_d}$ is the stress tensor. For the temperature, the conditions

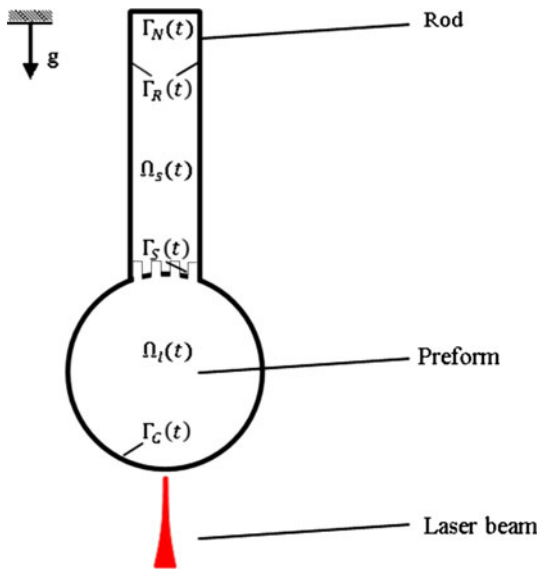

Fig. 2 Sketch of geometry

Table 2 Characteristic numbers

L	0.25×10^{-3} m	Characteristic length
L_{SG}	0.5×10^{-3} m	Characteristic length for conv. heat transfer
$\hat{t}$	1×10^{-3} s	Characteristic time
$U = \frac{L}{\hat{t}}$	0.25 m/s	Characteristic velocity
$\mathrm{Re} = \frac{\rho_l U L}{\mu}$	90	Reynolds number
$\mathrm{Pr} = \frac{\mu c_{p_l}}{\lambda_l}$	0.13	Prandtl number
$\mathrm{Bo} = \frac{\rho_l L^2}{\gamma}$	0.259×10^{-2}	Bond number
$\mathrm{We} = \frac{\rho_l U^2 L}{\gamma}$	0.066	Weber number
$\mathrm{Gr} = \frac{\rho_l^2 g \beta (T_m - T_a) L^3}{\mu^2}$	48.77	Grashof number
$\mathrm{Ste} = \frac{c_{p_l}(T_m - T_a)}{H_M}$	4.15	Stefan number

$$\frac{1}{\mathrm{RePr}}\partial_v T = \mathrm{La} I_l + \mathrm{Em}\left(T_a^4 - (T_m + T)^4\right) + \tilde{\alpha}_l (T_a - T) \quad \text{on } \Gamma_C(t), \tag{8}$$

$$\frac{1}{\mathrm{RePr}}\frac{\lambda_s}{\lambda_l}\partial_n T = \mathrm{La} I_l + \mathrm{Em}\left(T_a^4 - (T_m + T)^4\right) + \tilde{\alpha}_s (T_a - T) \quad \text{on } \Gamma_R(t), \tag{9}$$

$$\frac{1}{\mathrm{RePr}}\partial_v T = 0 \quad \text{on } \Gamma_N(t), \tag{10}$$

are imposed to include laser heating and heat losses due to radiation and forced convection. Due to the non-dimensional model approach, the laser number La

$$\mathrm{La} = \frac{I_{\max}}{\rho_l c_{p_l} U (T_m^* - T_a^*)},$$

the emissivity number Em

$$\mathrm{Em} = \frac{\epsilon k_{\mathrm{SB}} (T_m^* - T_a^*)^3}{\rho_l c_{p_l} U},$$

and the convective heat transfer coefficient $\tilde{\alpha}_{\{s,l\}}$

$$\tilde{\alpha}_{\{s,l\}} = \frac{\alpha L}{\lambda_{\{s,l\}} \mathrm{RePr}} = \frac{\lambda_{\mathrm{SG}} \mathrm{Nu}_{\mathrm{SG}} \mathrm{L}}{L_{\mathrm{SG}} \lambda_{\{s,l\}} \mathrm{RePr}}$$

are used, where $I_{\max}$ is the maximum intensity of the laser beam, ϵ is the emissivity and k_{SB} denotes the Stefan-Boltzmann constant. The parameter λ_{SG} denotes the thermal conductivity. $\mathrm{Nu}_{\mathrm{SG}}$ denotes the Nusselt number of the shielding gas.

It is pointed out that heat losses due to convection are considered by introducing a heat transfer coefficient in Eq. (8–10), which depends on the shielding gas, but not by simulating the shielding gas flow itself. In order to simplify the systematical parameter variation performed in Sect. 6.3, α is considered later as constant for each phase and does not change during the process due to the evolution of the melt and its shape.

For including phase transitions into the model, two different approaches are briefly presented which are combined for the numerical simulation of the process.

3.2.1 Enthalpy model

The enthalpy model, which has been considered in e.g. [7], is modified in order to model a problem including heat convection. The general idea of the enthalpy model is to formulate the energy balance in the whole domain $\Omega(t)$ which is given by

$$\partial_t H + u \nabla H - \frac{1}{\mathrm{RePr}} \Delta T = 0 \quad \text{in } \Omega(t), \tag{11}$$

with $u \equiv 0$ in $\Omega_s(t)$ and

$$T = f(H) := \begin{cases} \frac{\rho_s c_{p_s}}{\rho_l c_{p_l}} H, & H < 0 \\ 0, & H \in \left[0, \frac{1}{\mathrm{Ste}}\right] \\ H - \frac{1}{\mathrm{Ste}}, & H \geq \frac{1}{\mathrm{Ste}} \end{cases} \tag{12}$$

describing the temperature-enthalpy relation where H denotes the enthalpy density. By solving Eq. (11), the solid-liquid interface

$$\Gamma_S(t) := \{x \in \Omega(t) | T(x) = 0\}$$

is given implicitly. Consequently, the enthalpy model can naturally handle the nucleation and the vanishing of a liquid subdomain as well as multiple solid-liquid interfaces or a mushy region.

3.2.2 Sharp interface model

Another model applicable for problems with phase transitions is a sharp interface model, cf. [4]. In this approach, the solid-liquid interface $\Gamma_S(t)$ is defined as sharp boundary that is handled explicitly. On $\Gamma_S(t)$ the boundary conditions

$$u \cdot v = \left(1 - \frac{\rho_s}{\rho_l}\right) V_{\Gamma_S} \cdot v, \tag{13}$$

$$u - u \cdot v v = 0, \tag{14}$$

$$T = 0, \tag{15}$$

$$\frac{1}{\mathrm{RePr}}\left[(\nabla T)_l - \frac{\lambda_s \rho_l c_{p,l}}{\lambda_l \rho_s c_{p,s}} (\nabla T)_s\right] = \frac{1}{\mathrm{Ste}} V_{\Gamma_S} \tag{16}$$

are prescribed. The Stefan condition (16) reflects the thermal energy balance in the domain and is used to obtain the velocity V_{Γ_S} of the interface $\Gamma_S(t)$. Please note that by using this model, neither nucleation of melt nor topology changes can be handled.

4 Numerical aspects

4.1 Numerical approach

The process described by PDE-system (2–16) is implemented in a finite element method partly based on [3]. Within this method, the enthalpy model and the sharp interface model are combined in order to simulate phase transitions and to handle the interdependence of Stefan problem and Navier–Stokes equations with a free capillary surface.

The enthalpy FE method treats phase transitions implicitly by solving Eq. (11) on the whole domain. Consequently, the interface $\Gamma_S(t)$ is in general not given on mesh edges but intersects mesh elements. This offers a high flexibility but may introduce numerical difficulties regarding the computation of the fluid flow.

In the sharp interface model, the domain is separated in a liquid and a solid subdomain by the interface $\Gamma_S(t)$ which is represented by edges of elements. On each subdomain the heat equation is solved independently using an internal Dirichlet condition (15) at the interface. The jump of the temperature gradients across $\Gamma_S(t)$ is then used to compute its velocity, cf. Eq. (16). The outer geometry boundaries are moved accordingly to the deformation of the capillary surface $\Gamma_C(t)$ and the movement of the interface $\Gamma_S(t)$. By applying an ALE-approach, the interior mesh is moved as well, using an extension operator [4]. This method allows a very precise simulation but lacks on flexibility as it does not allow for topology changes like nucleation.

By coupling both methods, one can benefit from each method's advantages by avoiding their disadvantages. A detailed description of the numerical aspects of the finite element method and the coupling of the approaches is given in [11] and [12].

4.2 Finite element simulation

The material accumulation process using laser-based free form heading can be assumed to be rotational symmetric, if the laser is applied to a thin metallic wire coaxially. All numerical results presented in Sect. 6 are therefore simulated by using a 2D rotational symmetric approach.

The finite element simulation can be used for different purposes. In [12], the self-alignment property of the material accumulation process, which is shown in [2], is confirmed by simulation results. In [10], the micro-structure and the shape of experimental produced material accumulations are compared to simulation results and show a good agreement. As already pointed out, in this paper the energy dissipation is analyzed.

5 Experimental setup

For experiments, a rod with a diameter $d_0 = 0.5$ mm of chromium nickel steel 1.4301 (X5CrNi18-10) is used as wrought material. The rod is oriented coaxially to the laser beam, so that the laser beam interacts perpendicular with the surface of the rod. In order to achieve a high reproducibility of results, the face surface of the rod interacting with the laser beam is finely ground initially. As laser beam source, a fibre laser TruFiber 300 of Trumpf is used. Both, the specification of beam source as well as process parameters can be found in Table 3.

The operation device of the beam source allows adjusting the power of the laser pulse as well as the pulse duration. Therefore, the energy provided by the beam source can be set very precisely. The face surface of the rod is placed in focus layer initially but moving out of focus layer during the accumulation process due to the defocussing effect as described in Sect. 2. In order to prevent oxidation of rod material at elevated temperatures during the accumulation process and solidifying process, argon is used as shielding gas. Assuming a laminar gas flow, the velocity of shielding gas parallel to the symmetry axis of the rod is approximately 1.9 $\frac{\mathrm{m}}{\mathrm{s}}$. Figure 3 shows a schematic illustration of the experimental setup.

6 Results

6.1 Comparing experimental data with numerical results

The experimental data obtained by the parameters given in Table 3 are compared to the analytical model given in Sect.

Table 3 Specifications of the laser system and the used process parameters

Laser	Trumpf TruFiber 300
Laser type	Fibre laser
Wavelength	1085 nm
Focal distance	100 mm
Beam radius	0.02 mm
Divergence angle	40 mrad
Material	Steel 1.4301 (X5CrNi18-10)
Power	160 W
Pulse duration	{250, 500, 750, 1000} ms
Rod diameter	0.5 mm
Shielding gas	Argon
Shielding gas temperature T_{SG}	293 K
Shielding gas velocity	1.9 $\frac{\mathrm{m}}{\mathrm{s}}$

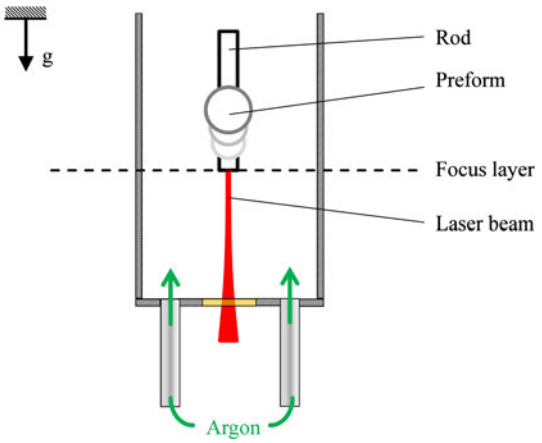

Fig. 3 Schematic illustration of experimental setup

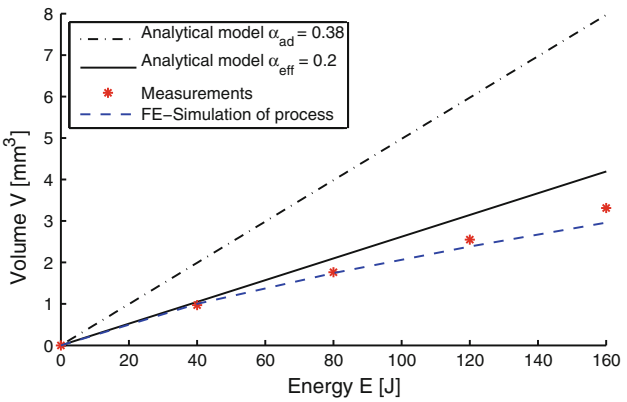

Fig. 4 Comparison of adiabatic model, experimental data and numerical results for specimen with rod diameter $d_0 = 0.5$ mm using the parameters given in Table 3

3.1 and to the results of the finite element simulation based on the continuum mechanical model from Sect. 3.2.

In Fig. 4, the volume of the material accumulation is plotted against the applied energy. According to Eq. (1), the analytical model predicts a linear relation between applied energy and generated volume of the material accumulation. The increase of the function depends on the choice of α_L.

Due to the fact that the analytical model is based on assuming adiabatic conditions, the value $\alpha_{ad} = 0.38$ corresponds to an adiabatic model of the process. The results obtained by this model can be seen as an upper bound of achievable results in laser-based free form heading. For a more realistic situation where heat losses are present, an adjusted value $\alpha_{eff} \approx 0.20$ is chosen [20] to consider energy dissipation empirically. Not surprisingly, the choice of α_{eff} gives a much better approximation of the process. However, the experimental data do not show a linear but only a monotone relation between applied energy and volume, whereas the increase in volume flattens for increasing energy. The differences between the experimental data and the analytical model are, of course, a consequence of the considerable simplifications made within the model and are to be expected.

In contrast to the analytical model, the finite element simulation fits the nonlinear behavior of experimental data very well. In detail, the volume of the preform as computed by the finite element simulation for an energy pulse up to 120 J differs only slightly from the experimentally determined values. For higher energy pulses, a small but increasing gap can be observed, i.e. the simulation overestimates the volume approximately by 10 % for an energy pulse of 160 J. The same behavior can be observed for other rod diameters with accordingly adapted energy pulses [15]. Possible reasons for the increasing gap between simulation results and experimental data are again the simplifications assumed in the model, e.g. the use of temperature-independent parameters. Additionally, discretization and approximation errors arise in the simulation approach.

6.2 Overview about heat losses arising during laser heating

6.2.1 Considered energy dissipation mechanisms

While measuring heat losses during the experiments precisely turns out to be almost impossible, the losses can be considered and quantified very easily by using a finite element simulation of the process. The mechanisms causing energy dissipation, which are considered in this paper, are radiation

$$\dot{Q}_{\mathrm{rad}}(t) = \int_{\Gamma_C(t)\cup\Gamma_R(t)} \epsilon\kappa_{\mathrm{SB}}\left(T(x,t)^4 - T_a(x,t)^4\right) do \qquad (17)$$

described by the Stefan-Boltzmann law, forced convection

$$\dot{Q}_{\mathrm{fc}}(t) = \int_{\Gamma_C(t)\cup\Gamma_R(t)} \alpha(T(x,t) - T_{\mathrm{SG}}(x,t))\, do \qquad (18)$$

caused by the shielding gas acting on the material surface, and thermal conduction

$$\dot{Q}_{\mathrm{tc}}(t) = \int_{\Gamma_S(t)} \lambda\nabla T|_{\Omega_s}\, do \qquad (19)$$

of heat into the rod. Due to the fact that radiation and convection are considered as fluxes on the rod surface as well as on the melt surface, $\dot{Q}_{\mathrm{tc}}(t)$ does not describe the actual amount of losses caused by thermal conduction as they influence the process. Therefore, instead of using

Table 4 Process parameters: Influence of irradiation time and laser power

Power $P_{1,2}$	160 W	80 W
Pulse duration $t_{f1,f2}$	500 ms	1,000 ms
Rod diameter d_0	0.5 mm	
ϵ	0.6	
α	200 W/m^{2}K	
α_{laser}	0.38	

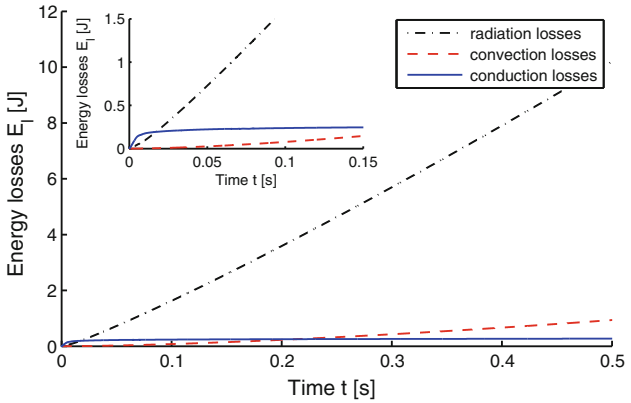

Fig. 5 Heat losses arising during melting process in Joule for $P = 160$ W, $t_f = 0.5$ s, $\alpha = 200\ \frac{\text{W}}{\text{m}^2\text{K}}$, $\lambda_s = 15\ \frac{\text{W}}{\text{mK}}$ and $\epsilon = 0.6$

Eq. (19) the energy dissipation due to thermal convection is considered not as flux but as amount of energy

$$E_{\text{tc}}(t) = \int_{\Omega_s(t)} c_{p_s}\lambda_s(T(x,t) - T_a(x,t))dx. \tag{20}$$

which is in the rod at time t. The losses (17), (18) are accumulated over the irradiation time t_f

$$E_{\text{rad}}(t) = \int_{t_0}^{t} \dot{Q}_{\text{rad}}(\tau)d\tau \tag{21}$$

$$E_{\text{fc}}(t) = \int_{t_0}^{t} \dot{Q}_{\text{fc}}(\tau)d\tau \tag{22}$$

and added to the energy in the rod in order to get the overall energy dissipated during laser heating

$$E_{\text{l}}(t_f) = E_{\text{rad}}(t_f) + E_{\text{fc}}(t_f) + E_{\text{tc}}(t_f). \tag{23}$$

6.2.2 *Influence of irradiation time and laser power*

The heat losses arising in laser based free form heading are not only dependent on the amount of energy but also on the experimental setup. By changing the irradiation time t_f while maintaining the applied energy, the total amount of

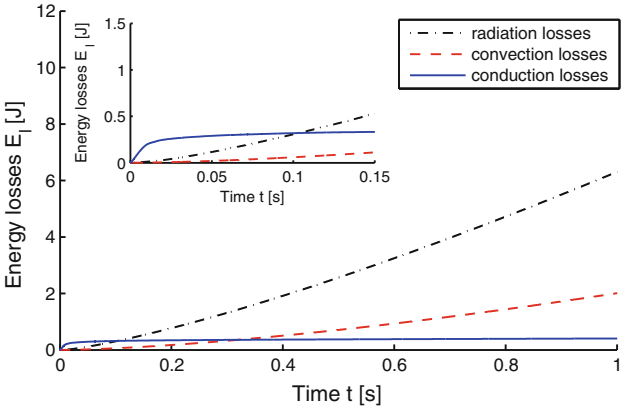

Fig. 6 Heat losses arising during melting process in Joule for $P = 80$ W, $t_f = 1.0$ s, $\alpha = 200\ \frac{\text{W}}{\text{m}^2\text{K}}$, $\lambda_s = 15\ \frac{\text{W}}{\text{mK}}$ and $\epsilon = 0.6$

heat losses arising during the laser heating process and the proportions of the losses can be influenced very much. This effect is exemplary shown for an energy pulse $E = 80\,\text{J} = P_1 \cdot t_{f_1} = P_2 \cdot t_{f_2}$ obtained by two different irradiation times t_{f_1} and t_{f_2} with accordingly adapted laser powers P_1 and P_2, cf. Table 4.

The accumulated amount of dissipated energy due to radiation $E_{\text{rad}}(t)$ (21), convection $E_{\text{fc}}(t)$ (22), and thermal conduction $E_{\text{tc}}(t)$ (20) arising during irradiation (t_0, t_f) for both experimental setups are shown in Figs. 5 and 6. Please note that due to absorption coefficient $\alpha_{\text{laser}} = 0.38$, the energy which is actually incoupled into the rod is not 80 Joule but 30.4 Joule.

For both experimental setups, it can be seen that the most important heat loss mechanism is radiation. Energy dissipation due to forced convection, which is caused by shielding gas acting on the material surface, and thermal conduction are less important for the given parameters. But if comparing the total amount of dissipated energy and its origin, it can be seen that the values and the proportion of the energy dissipation significantly differ during the laser heating period. If applying the energy pulse $E_1 = P_1 \cdot t_{f_1}$ to the work-piece, the amount of total dissipated energy is approximately 11.4 Joule, while the value decreases around 24% to round about 8.7 Joule, if using $E_2 = P_2 \cdot t_{f_2}$. This effect is a result of the very different temperature distributions arising in both setups. Because of the high laser power P_1, the temperatures arising during the process are very high which cause a high radiation because of the 4th power of the temperature in the Stefan-Boltzmann law. On the contrary, if applying the laser power P_2 for the longer time period t_{f_2} to the rod, the more energy is conducted into the rod leading to lower temperatures in the melt and thereby reducing the amount of energy that is radiated. Furthermore, the nucleation takes longer compared to the use of P_1.

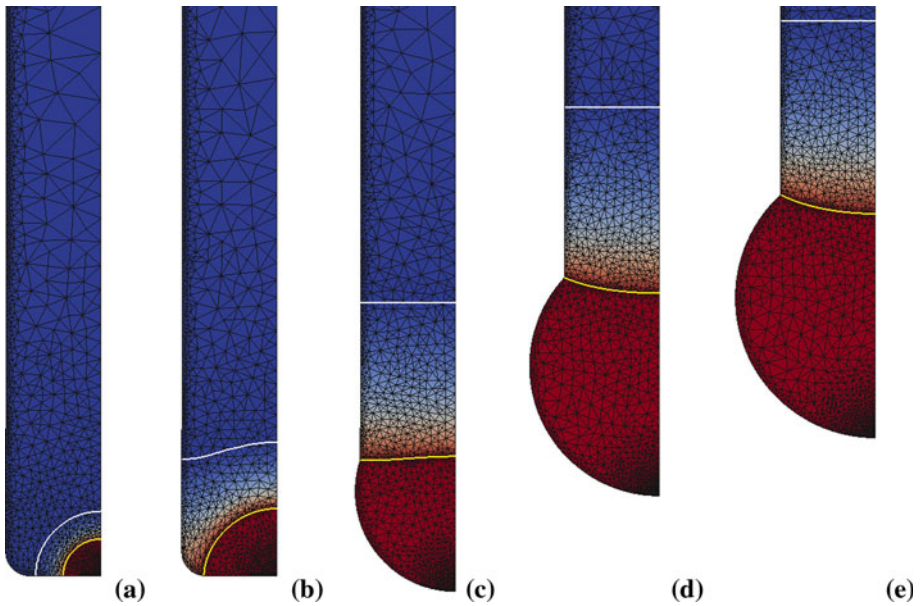

Fig. 7 Nucleation of the melt until it forms spherically. Time steps $t = 0.0005s$, $t = 0.0050s$, $t = 0.0150s$, $t = 0.0250s$ and $t = 0.0400s$

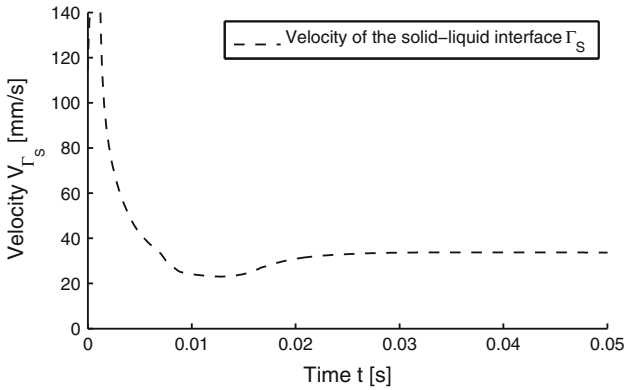

Fig. 8 Velocity of the solid-liquid interface Γ_S during laser heating process

A very interesting observation concerns thermal conduction losses. The results indicate that the influence of thermal conduction is strong only at the very beginning of the process. After some initial time, the energy dissipation due to heat conduction is almost constant, cf. the magnified plots in Figs. 5 and 6. This effect is caused by the evolution of the heat affected zone within the rod which depends strongly on the interface's velocity V_{Γ_S} and its acceleration respectively its deceleration. For the laser heating process using the parameters $E = P_1 \cdot t_{f_1}$, this behavior is further visualized in Figs. 7 and 8. In Fig. 7, the nucleation of the melt is shown until it shapes spherically. In addition to the interface Γ_S, the temperature-isoline that corresponds to a temperature of $T_{\text{haz}} = 100\ ^\circ\text{C}$ is indicated. The zone between both isolines is named *heat affected zone*. Figure 8 visualizes the corresponding velocity of the interface during the whole irradiation time t_{f_1}.

It can be seen in Fig. 8 that during nucleation of the melt, the velocity V_{Γ_S} resp. the acceleration of the interface is very high, causing a growing heat affected zone and, consequently, an increasing energy dissipation due to heat conduction. After a sufficient amount of melt is generated, see Fig. 7c, the melt begins to shape as a sphere due to size effects and the velocity of the interface decreases to approximately 31 $\frac{\text{mm}}{\text{s}}$. In the following, the velocity of the interface is almost constant and the heat affected zone stabilizes, cf. Fig. 7d, e.

At this point, it is stressed that in this paper, energy dissipation is analyzed only for the laser heating process which does not include the solidification process. Consequently, the temperatures in the melt for both setups $E = P_1 \cdot t_{f_1}$ and $E = P_2 \cdot t_{f_2}$ differ significantly after switching off the laser source causing a different cooling down behavior. If the whole process including the solidification is considered, the amount of dissipated energy is of course almost the same for both simulations, due to the fact that the same energy is applied to the rod. This is shown in Fig. 9.

Furthermore, it has to be noted that all observations and conclusions are true only if the experimental setup is varied within a reasonable range. For process setups with very small laser power, all energy is conducted into the rod and no material melts. Such situations are not considered in this paper.

In the remainder of this section, the initial parameters given in Table 5 are used and the parameters for the emissivity ϵ, the heat transfer α and the thermal conductivity λ are varied to analyze their influence on the energy dissipation $E_I(t_f)$ of the material accumulation process

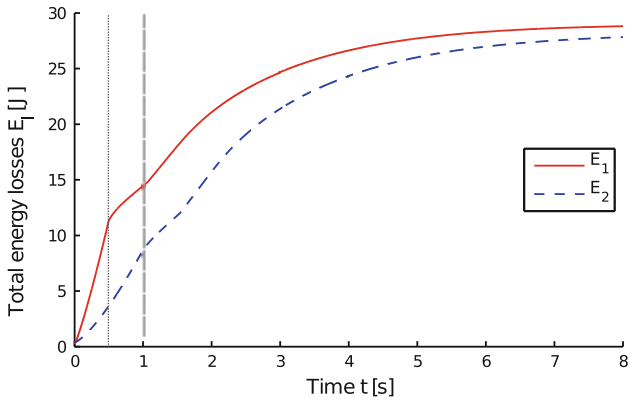

Fig. 9 Comparison of the total amount of energy E_l dissipated during the whole process including the solidification process for both process setups. The *vertical lines* indicate the irradiation times $t_{f_1} = 0.5\,\text{s}$ and $t_{f_2} = 1.0\,\text{s}$

Table 5 Process parameters for the study of heat losses

Power P	160 W
Pulse duration t_f	500 ms
Rod diameter d_0	0.5 mm
ϵ	0.6
α	200 W/m^{2}K
α_{laser}	0.38

during laser heating. In addition to the values in Joule, the losses are presented as percentages of the overall accumulated heat dissipation

$$E_p = 100 \cdot \frac{E_{\{\text{rad,fc,tc}\}}(t_f)}{E_l(t_f)} \tag{24}$$

arising during the laser heating time as well, to take the nonlinear coupling of all heat losses into account. This is important, as the variation of a single parameter affects not only the amount of energy dissipated by the other effects but also the amount of the overall dissipated energy.

6.3 Systematic parameter variation in numerical model to study heat losses

6.3.1 Influence of the emissivity ϵ

The emissivity coefficient ϵ is varied within the range of 0.5 to 0.9 whereas the coefficients $\alpha = 200\ \frac{\text{W}}{\text{m}^2\text{K}}$ for the convective heat transfer and $\lambda_s = 15\ \frac{\text{W}}{\text{mK}}$ resp. $\lambda_l = 35\ \frac{\text{W}}{\text{mK}}$ for the thermal conductivity remain unchanged. The simulated energy dissipation in Joule for $\epsilon \in \{0.5, 0.55, 0.6, 0.65, 0.7, 0.75, 0.8, 0.85, 0.9\}$ is shown in Fig. 10a. It can be seen for the considered values that the heat losses increase approximately linear but not proportional to increasing emissivity. This behavior can also be

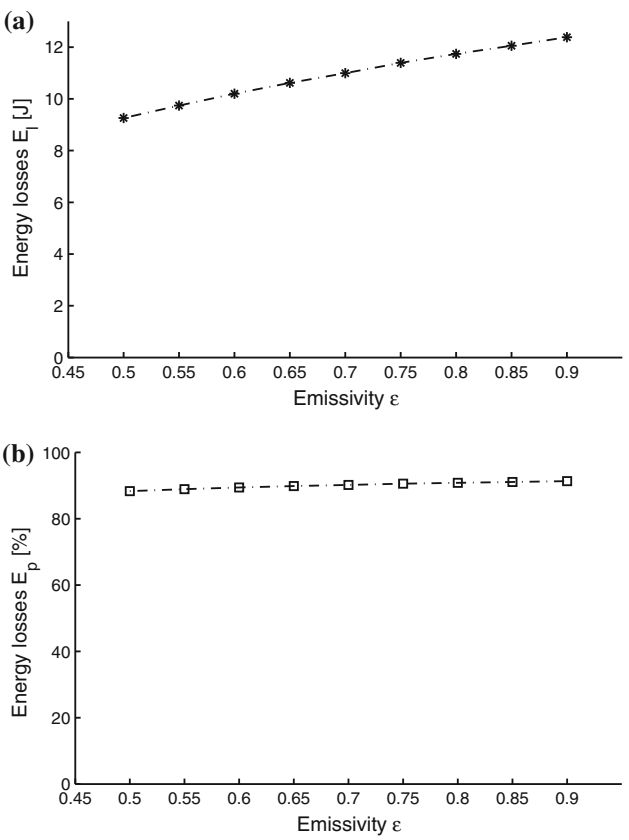

Fig. 10 Accumulated energy losses due to radiation in Joule (**a**) and in percent subject to the accumulated overall heat losses (**b**) for $\alpha = 200\frac{\text{W}}{\text{m}^2\text{K}}, \lambda_s = 15\ \frac{\text{W}}{\text{mK}}, \lambda_l = 35\ \frac{\text{W}}{\text{mK}}$ and $\epsilon \in \{0.5, 0.55, 0.6, 0.65, 0.7, 0.75, 0.8, 0.85, 0.9\}$

seen in Fig. 10b which visualizes the heat losses due to radiation subject to the accumulated overall heat losses arising during the laser heating. It can be seen that the increase of the parameter for emissivity from 0.5 up to 0.9 leads only to a rise from 88 to 91 % of the proportion of the accumulated overall heat losses. This is mainly due to the high proportion it represents for the accumulated energy dissipation.

Unfortunately, determining the emissivity ϵ by experiments or by models is very difficult. Moreover, it can hardly be influenced in the experiments and, consequently, cannot be avoided. The only aspect which can be controlled is the ambiance temperature, cf. Eq. (17). Typically, the parameter ϵ is approximated for the model by performing parameter identification. As shown in Fig. 10, a small variation in ϵ does influence the process behavior only slightly.

6.3.2 Influence of the heat transfer coefficient α

The coefficient α describes the heat transfer between the material and the shielding gas. In order to quantify its

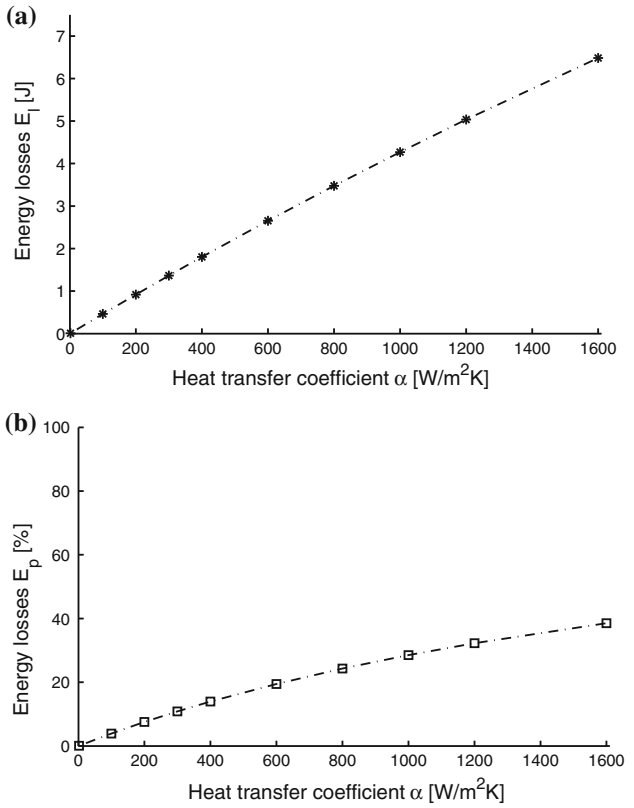

Fig. 11 Accumulated energy losses due to forced convection in Joule (**a**) and in percent subject to the accumulated overall heat losses (**b**) for $\epsilon = 0.6, \lambda_s = 15\ \frac{\mathrm{W}}{\mathrm{mK}}, \lambda_l = 35\ \frac{\mathrm{W}}{\mathrm{mK}}$ and $\alpha \in \{2, 100, 200, 300, 400, 600, 800, 1000, 1200, 1600\}\ \frac{\mathrm{W}}{\mathrm{m^2K}}$

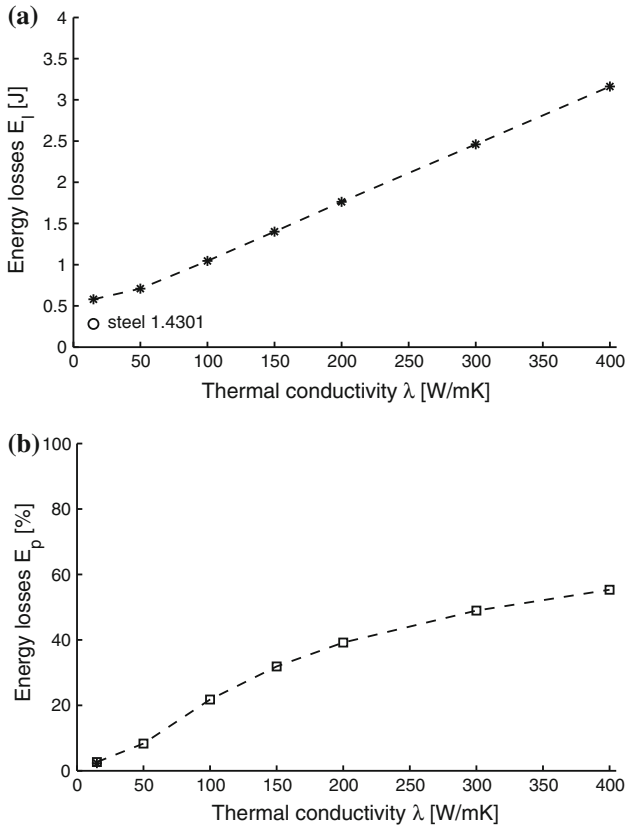

Fig. 12 Accumulated energy losses due to thermal conductivity in Joule (**a**) and in percent (**b**) for $\lambda \in \{15, 100, 150, 200, 250, 300, 400\}$

influence on the overall heat losses, the material accumulation process is simulated with $\epsilon = 0.6$ and $\lambda_s = 15\ \frac{\mathrm{W}}{\mathrm{mK}}$ resp. $\lambda_l = 35\ \frac{\mathrm{W}}{\mathrm{mK}}$ for $\alpha \in \{2, 100, 200, 300, 400, 600, 800, 1000, 1200, 1600\}\ \frac{\mathrm{W}}{\mathrm{m^2K}}$, where $\alpha = 2\ \frac{\mathrm{W}}{\mathrm{m^2K}}$ corresponds to a process with almost no shielding gas, $\alpha = 200\ \frac{\mathrm{W}}{\mathrm{m^2K}}$ corresponds to argon with 2.9 $\frac{\mathrm{m}}{\mathrm{s}}$ and $\alpha = 1600\ \frac{\mathrm{W}}{\mathrm{m^2K}}$ is possible if using helium with a very high outflow velocity of more than 10 $\frac{\mathrm{m}}{\mathrm{s}}$. The energy dissipation caused by convection is visualized in Fig. 11. It can be seen in Fig. 11a that the heat losses in Joule rise almost linearly with increasing α for the investigated parameter range. However, the proportion of energy that is lost due to convections rises not only monotonically dependent on α, but also the growth factor decreases with increasing α as shown in Fig. 11b. This flattening course of the graph indicates that the heat losses caused by convection are becoming of lesser importance in relation to the overall energy dissipation. This reflects the Dirichlet boundary condition arising from Eq. (18).

In the experimental setup, the influence of the heat transfer can be controlled very well, e.g. by the choice of shielding gas or its outflow velocity. However, the use of shielding gas is necessary to prevent oxidation of the specimen during the process and therefore performing experiments without shielding gas is not advisable.

6.3.3 Influence of the coefficient of thermal conductivity λ

The coefficient of the thermal conductivity λ quantifies the property of a material to conduct heat. In order to obtain its influence, λ is varied as $\lambda \in \{15, 50, 100, 150, 200, 300, 400\}$. Within this range, the values of the most common materials are included for example the thermal conductivity of zinc $\lambda_z = 113$, aluminum $\lambda_a = 230$, gold $\lambda_g = 317$ and copper $\lambda_c = 398\ \frac{\mathrm{W}}{\mathrm{mK}}$. For simplification, the thermal conductivity in liquid and solid phase are assumed to the be equal in this paragraph.

The thermal conductivity is a material property and cannot be changed. Therefore, one possibility to reduce heat losses due to thermal conduction during the process is to heat up the material, e.g. by applying a small energy pulse to the rod, before the process starts in order to decrease the temperature difference in Eq. (20). However, it is rather unlikely that the total efficiency of the process can be increased by this procedure due to possibly high costs during the heat-up phase.

The simulation results for the different thermal conductivities are shown in Fig. 12. Therein, an linearly increasing behavior of the losses in Joule for increasing thermal conductivity can be observed, cf. Fig. 12a. Additionally, the value for steel 1.4301 with the correct thermal conductivity in liquid and solid is marked in the figures. The very small kink between $\lambda = 15\ \frac{\mathrm{W}}{\mathrm{mK}}$ and $\lambda = 50\ \frac{\mathrm{W}}{\mathrm{mK}}$ is most certainly caused by effects during the nucleation of the melt. Interestingly, when considering the amount of losses caused by thermal conduction in relation to the overall losses, cf. Fig. 12b, the losses increase only monotonically showing a tendency to a logistic function.

7 Summary

In this paper, the energy dissipation of a laser-based free form heading process is investigated. Therefore, the process is modeled in a continuum mechanical framework and implemented in a finite element method for a numerical simulation. An indication of the high approximation quality of this approach is briefly given by comparing numerical results to experimental data. By using this simulation the heat losses can be quantified very easily contrary to measuring them during the experiments. In order to identify the influence of radiation, thermal conduction, and heat losses due to convection on the energy dissipation, the relevant parameters are varied systematically.

By doing so, it turns out that for the considered experimental setups and material properties, up to 90 percent of the overall heat losses arising during laser heating are caused by radiation making the emissivity the most important energy loss in laser-based free form heading. In contrast, only 5 to 10 percent of the heat losses are caused by convection and even less energy proportion of around 3 percent is dissipated by thermal conduction.

A high influence of the emissivity is to be expected because of the high temperatures arising during the process entering the Stefan-Boltzmann law, which describes heat losses caused by radiation, by the power of 4. However, the relatively small impact of the increasing emissivity on the accumulated overall energy dissipation is surprising. Another interesting result of the parameter variation is the fact that energy dissipation due to thermal conduction are almost constant after a very short time period when the nucleation of a sufficient amount of melt has taken place.

Acknowledgments The authors gratefully acknowledge the financial support by the DFG (German Research Foundation) for the subproject A3 within the Collaborative Research Center (CRC) 747 “Mikrokaltumformen - Prozesse, Charakterisierung, Optimierung”. Further, we want to thank the AG Bänsch from the University of Erlangen-Nürnberg for cooperation.

References

1. Bristeau MO, Glowinski R, Periaux J (1987) Numerical methods for the Navier–Stokes equations. Application to the simulation of compressible and incompressible flows. Comput Phys Rep 6:73–188
2. Brüning H, Vollertsen F (2012) Self-aligning capability of laser based free form heading process. In: Proceedings of 11th international scientific conference MMA—advanced production technologies, pp 427–430
3. Bänsch E (2001) Finite element discretization of the Navier–Stokes equations with a free capillary surface. Numer Math 88(2):203–235
4. Bänsch E, Paul J, Schmidt A (2013) An ALE finite element method for a coupled Stefan problem and Navier–Stokes equations with free capillary surface. Int J Numer Methods Fluids 71:1282–1296
5. Dausinger F (1995) Strahlwerkzeug Laser: Energieeinkopplung und Prozesseffektivität. B. G. Teubner
6. Eichenhüller B, Engel U, Geiger M (2010) Microforming and investigation of parameter interactions. Prod Eng 4(2–3):135–140
7. Elliot CM (1981) On the finite element approximation of an elliptic variational inequality arising from an implicit time discretization of the Stefan problem. IMA J Numer Anal 1:115–125
8. Gale W, Totemeier T (2003) Smithells metals reference book. Elsevier Science, Amsterdam
9. Geiger M, Kleiner M, Eckstein R, Tiesler N, Engel U (2001) Microforming. CIRP Ann Manuf Technol 50(2):445–462
10. Jahn M, Luttmann A, Schmidt A (2012) A FEM simulation for solid-liquid-solid phase transitions during the production of micro-components. In: Proceedings of 11th international scientific conference MMA—advanced production technologies
11. Jahn M, Luttmann A, Schmidt A, Paul J (2012) Finite element methods for problems with solid-liquid-solid phase transitions and free melt surface. PAMM 12(1):403–404
12. Jahn M, Schmidt A (2012) Finite element simulation of a material accumulation process including phase transitions and a capillary surface. Tech. Rep. 12-03, ZeTeM, Bremen
13. Messner A (1998) Kaltmassivumformung metallischer Kleinstteile: Werkstoffverhalten, Wirkflächenreibung, Prozeßauslegung. Fertigungstechnik—Erlangen, Meisenbach
14. SA LM (2013) Stahl 1.4301. Tech. Rep. 2013/01, Lamineries MATTHEY SA, Lamineries MATTHEY SA, CH-2520 La Neuveville
15. Sakkiettibutra J, Vollertsen F (2009) Größeneffekte beim Stauchmechanismus am Beispiel geometrisch skalierter Brückenaktuatoren. Größeneinflüsse bei Fertigungsprozessen, BIAS Verlag, Bremen, pp 97–116
16. Stephen A, Brüning H, Vollertsen F (2011) Fokuslagensteuerung beim laserbasierten Stoffanhäufen. In: 5. Kolloquium Mikroproduktion und Abschlusskolloquium SFB 499, KIT Scientific Publishing, Karlsruhe, pp 155–160
17. Stephen A, Vollertsen F (2011) Influence of the rod diameter on the upset ratio in laser-based free form heading. Steel Research Int., Special Edition: 10th international conference on technology of plasticity (ICTP) pp 220–223
18. Vollertsen F (2013) Micro metal forming. Lecture notes in production engineering. Springer, London
19. Vollertsen F, Walther R (2008) Energy balance in laser based free form heading. CIRP Ann 57:291–294
20. Walther R (2009) An enhanced model for energy balance in laser-based free form heading. J Micromech Microeng 19:1–6